Arabian Journal for Science and Engineering (2021) 46:5489–5503
https://doi.org/10.1007/s13369-020-05015-2

RESEARCH ARTICLE-CHEMISTRY

Synthesis, Characterization and Corrosion Inhibition Performance of Glycine-Functionalized Graphene/Fe_3O_4 Nanocomposite (Gr/Fe@Gly NC) for Mild Steel Corrosion in 1 M HCl

R. Aslam[1] · M. Mobin[1] · M. Shoeb[1] · M. Parveen[1] · S. Zehra[1] · J. Aslam[2]

Received: 10 May 2020 / Accepted: 4 October 2020 / Published online: 21 October 2020

Abstract

We have synthesized a ternary glycine-functionalized graphene/Fe_3O_4 nanocomposite referred as Gr/Fe@Gly NC which was characterized by fourier transform infrared spectroscopy analysis (FT-IR), X-ray diffraction, high-resolution scanning electron microscopy/energy-dispersive X-ray spectroscopy (HR-SEM/EDS) and the transmission electron microscopy. The effectiveness of synthesized nanocomposite as anticorrosive material for mild steel in the acid medium was assessed using weight loss, electrochemical impedance spectroscopy (EIS) and potentiodynamic polarization (PDP) complemented with FT-IR and SEM studies. The results of weight loss study depicted its effectiveness and stability up to 60 °C at very low concentrations. FT-IR and SEM studies supported the existence of a protective film on the inhibited steel surface. The adsorption followed the Langmuir adsorption isotherm; as such, it approximated and defined the thermodynamic and kinetic parameters governing the adsorption process. ANOVA statistical check confirmed that there is statistically no significant difference between the inhibition efficiencies obtained through weight loss, PDP and EIS techniques.

Keywords Nanocomposite synthesis · Acid corrosion · Inhibition · Graphene–Fe_3O_4@glycine nanocomposite

1 Introduction

Metal corrosion protection is essential to ensure valuable part and longevity of the device, thus avoiding economic losses, devastating accidents caused by corrosion and the negative environmental impacts. Mild steel (having a carbon content up to 0.3%) has high mechanical properties, is relatively inexpensive and is used in many industrial applications [1, 2]. However, mild steel is prone to undergo corrosion which is triggered by many environmental factors like moisture, oxygen and electrolyte [3]. A well-established strategy for corrosion protection is the use of corrosion inhibitors in corrosive conditions. However, the toxicity of most of the corrosion inhibitors discharged into the environment posed a serious threat to the health and the environment. Scientists and engineers have been researching alternative sources of corrosion inhibitors to develop environmentally friendly goods that can achieve maximum efficiency and reduce effects on nature and humanity [3].

Nanotechnology has played a crucial role in the development of innovative technological advances to control steel corrosion in the last two decades [3–5]. Quadri et al. [6] synthesized nanocomposites of ZnO with poly(ethylene glycol,), poly-(vinylpyrrolidone) and polyacrylonitrile and studied their anticorrosive properties for mild steel in 5% HCl solution using OCP, PDP, LPR, EIS measurements and SEM study. The observation of the results suggested that the NC exhibits mix-type inhibition tendency; the ZnO/PEG and ZnO/PVP principally affect the anodic reaction, whereas the cathodic reactions are mainly affected by ZnO/PAN. The order of inhibition efficiency obtained by the ZnO/polymer nanocomposites tested in 5% HCl for mild steel corrosion at a maximum concentration of 1000 ppm from the EIS test was as follows: ZnO/PVP > ZnO/PAN > ZnO/PEG. Following the Langmuir adsorption isotherm model, ZnO/polymer nanocomposites adsorb onto the surface of mild steel. Solomon et al. [7] prepared AgNPs/chitosan composite and documented their strength as an inhibitor using electro-

✉ M. Mobin
drmmobin@hotmail.com

[1] Corrosion Research Laboratory, Department of Applied Chemistry, Faculty of Engineering and Technology, Aligarh Muslim University, Aligarh 202002, India

[2] Department of Chemistry, College of Science, Taibah University, Yanbu, Al-Madina 30799, Saudi Arabia

chemical impedance spectroscopy (EIS), potentiodynamic polarization (PDP), dynamic electrochemical impedance spectroscopy (DEIS) and weight loss (WL) methods complemented by surface morphological using energy-dispersive X-ray spectroscopy (EDS), atomic force microscopy (AFM) and scanning electron microscopy (SEM) for St37 steel in 15% HCl solution at 25 and 60 °C. AgNPs/chitosan composite adsorption includes processes of physisorption with chemisorption and follows the Temkin isotherm model of adsorption. The PDP results showed that AgNPs/chitosan composite acts as a cathodic inhibitor. Atta et al. [8] reported a remarkable improvement in the corrosion resistance of mild steel in 0.1 N HCl medium due to the incorporation of magnetite into the Myrrh matrix.

As far as carbonaceous material is concerned, graphene is famous for its impressive electrical, mechanical and chemical characteristics with a wide specific surface area [9], but the non-polar nature of graphene and functional group deficiency limits its solubility in aqueous media, making it a great coating substance [10]. This poor solubility of graphene in aqueous media imposes a practical restriction in the realization of graphene as a corrosion inhibitor. In contrast, graphene oxide (GO) shows considerably better solubility in the aqueous media due to presence of several hydrophilic groups, i.e., hydroxyl, epoxide, carbonyl and carboxyl groups [11]. There are few reports on the corrosion inhibition behavior of chemically altered GO [12–14]. The excellent inhibition behavior of chemically altered GO at considerably low concentrations prompted our attention to explore this fascinating nanomaterial to inhibit mild steel corrosion in acidic medium. However, the major issue in utilizing graphene family, i.e., graphene, graphene oxide (GO) and reduced graphene oxide (rGO) nanomaterials, is their toxic effects [15]. Graphene/inorganic nanoparticles-based nanocomposites have attracted tremendous attention as a new class of hybrid materials. Magnetic nanoparticles with tailored properties have found various important applications in nanomedicine, electronics, separation technology, catalysis and magnetic sealing. Among them, magnetite (Fe_3O_4) nanoparticles are one of the attractive materials because of its very low toxicity, natural abundance and low cost [10]. Apart from enhancing the properties of graphene, the NPs also act as stabilizers against the aggregation of individual graphene sheets, which is greatly caused by the strong van der Waals interactions between graphene layers. However, graphene/inorganic nanoparticles-based nanocomposites prepared from chemical methods usually suffer from irreversible aggregations and poor dispersibility of nanoparticles on the surface of graphene, which require surface functionalization of the nanoparticles and/or graphene sheets to enhance processability of these materials. It is reported in the previous studies [16] that GO can be reduced after the covalent functionalization with a hydrophilic functional group/molecule or a charged moiety to impart water dispersity. Furthermore, majority of the chemicals involved in the functionalization of nanocomposites are highly toxic in nature, which are harmful to both environment and human life [17]. In order to minimize their hazardous effects, increasing efforts have been put to devise environmentally friendly reducing agent(s)/protocols for their synthesis on a large scale. Some of the environmentally friendly reducing agents employed are: reducing sugar, starch-based materials, ascorbic acid and amino acids [17]. Among these, amino acids have gained significant attention due to their cost-effectiveness, easy availability, bulk amount and biocompatible nature. Since glycine has a small side chain of only one hydrogen atom, it can fit into hydrophobic environments of graphene easily [18]. Moreover, the low price and non-hazardous features of glycine contribute to its usefulness as an appropriate reducing agent for preparation of graphene. Furthermore, glycine not only acts as reducing agents but also functions as in situ functionalization ligand which facilitated the binding of Fe_3O_4 NPs onto the surface of graphene sheets. Glycine further exhibited dual functions: (a) it assisted the dispersion of GO–Fe_3O_4 NC in water, and (b) the glycine endowed the NC with a corrosion inhibition effect [18].

In this context, nanocomposite of glycine-functionalized graphene–Fe_3O_4 (Gr/Fe@Gly) has been prepared through easy and facile procedure. The synthesized Gr–Fe@Gly NC was characterized using X-ray diffraction (XRD), Fourier transform infrared (FT-IR) spectroscopy, SEM/EDX and transmission electron microscopy (TEM) techniques. The anticorrosive behavior was examined employing weight loss, PDP, EIS, FT-IR and SEM studies. To the best of our knowledge, Gr–Fe@Gly NC's capacity for corrosion inhibition has not been claimed until now. The NC reported here has demonstrated to be an interesting class of novel and potentially environment-friendly corrosion inhibitor with admirable potency. Further, the cost-effectiveness and practical applicability of studied Gr–Fe@Gly NC were confirmed by comparing its inhibition performance with the already reported literature based on functionalized graphene.

2 Experimental

2.1 Preparations of Test Solution and Specimens

The rectangular mild steel coupons (exposed surface area 10.9 cm^2) with composition reported in our earlier publications [19, 20] were used in the weight loss measurements and surface analyses, whereas circular coupons of mild steel with exposed surface of 1 cm^2 were used in electrochemical measurements. Prior to commencement of experiments, the steel coupons were abraded with different grades of sandpapers (320, 400, 600 and 1200 grit size) to remove scaling, oxide layer and surface contamination, until the surface of the metal was obtained as glossy as a mirror. Subsequently, the coupons were degreased and cleaned with ethanol and acetone. Then, the coupons were washed with deionized water, dried in hot air and then used for further experiments [21].

The HCl solution was prepared with deionized water by diluting the concentrated HCl (37%, reagent grade) to a concentration of 1 M. The different dosage of nanocomposite ranging from 1 to 500 ppm was added into the acid solution. Acidic solution without adding nanocomposite dose was also prepared as a reference.

2.2 Synthesis and Characterization of Gr/Fe@Gly NC

2.2.1 Gr/Fe NC Synthesis

GO has been synthesized by oxidizing natural graphite powder (20 μm mesh, Sigma-Aldrich) in accordance with the manner described in our earlier research articles [22–24]. The graphene Fe_3O_4 NC was synthesized utilizing hydrothermal method. Typically, graphene oxide (2 mg mL^{-1}) was dispersed in double distilled water and sonicated using ultrasonic bath. The mixture of $FeCl_2{\cdot}4H_2O$ (0.005 mol) and $FeCl_3{\cdot}6H_2O$ (0.015 mol) was added under ultrasonication for 2 h into the graphene oxide dispersion and stirred for 60 min. An aqueous ammonia (1.5 M) solution was added drop-wise under vigorous stirring for 2 h. The stable suspension was enclosed in a 100-mL Teflon-lined autoclave and treated for 12 h at 180 °C hydrothermally. After that, the samples were collected using centrifugation method and dried under vacuum condition [25].

2.2.2 Gr/Fe@Gly NC Synthesis

The graphene Fe_3O_4 nanocomposite (Gr/Fe NC) obtained was coated with glycine by means of ultrasonic process (Fig. 1). First, Gr/Fe NC (100 mg) was dispersed 20 min by ultrasonication in 50 mL of distilled water. This suspension was then added to a solution of 100 mL of 10% glycine (in 1% acetic acid). Next, the sample was continuously stirred for 72 h at 40 °C followed by ultrasonication for another 120 min. Subsequently, the obtained Gr/Fe@Gly NC was rinsed three times with distilled water to eliminate excessive glycine and allowed to settle down under an external magnetic field and subjected to drying. To improve the dispersibility of Gr/Fe@GlyNC in aqueous media, the coated Gr/Fe@GlyNC was further functionalized with glycine. The obtained Gr/Fe@GlyNC was next properly re-dispersed in 10% glycine solution [26, 27].

2.2.3 Gr/Fe@GlyNC Characterization

The FT-IR spectrum of Gr/Fe@GlyNC was documented in the range of 4000–400 cm^{-1} utilizing PerkinElmer spectrometer through the KBr pellet method. The elemental composition of Gr/Fe@Gly NC was determined using an EDAX model, INCA Oxford, coupled to the SEM JEOL JSM-6610 LV. The morphology of Gr/Fe@Gly NC was observed by TEM, JEOL 100/120 kV model.

2.3 Corrosion Evaluation Methods

2.3.1 Weight Loss Method

Measurements of weight loss were made in triplicate using the mechanically polished and pre-weighed mild steel coupons, mentioned above. The coupons were immersed in a solution of 250 mL of 1 M HCl solution in the presence or absence of various dosages of Gr/Fe@Gly NC for 6 h at 30–70 °C in a temperature regulated water bath. The specimens were thoroughly cleaned with distilled water immediately after each experiment and dried and then accurately weighed using a digital balance with 0.1 mg precision.

The corrosion rate and efficiency of inhibition (η_w%) were calculated following the equations reported in the previous literature [19, 20, 28].

2.3.2 Electrochemical Method

The inhibitive behavior of studied Gr/Fe@Gly NC in the 1 M HCl solution was evaluated by employing PDP and EIS measurements. In this regard, three electrodes were added which included the saturated Ag/AgCl reference electrode, the Pt wire counter electrode and the mild steel working electrode. All the measurements were executed via Autolab potentiostat/galvanostat Model 128 N with inbuilt impedance analyzer FRA 2. EIS measurements with sinusoidal wave of 10 mV perturbation at open circuit potential (OCP) were performed in the frequency array of 10^{-2}–10^5 Hz. Using the Nova software, the impedance spectra obtained have been detailed. The test for potentiodynamic polarization was carried out in OCP ± 250 mV potential range and 0.001 V s^{-1} sweep rate.

2.3.3 FT-IR Measurement

FT-IR spectra were registered using PerkinElmer's spectrometer ('Spectrum Two' with 0.5 cm^{-1} spectral resolution) equipped with Spectrum Software in the 4000 to 400 cm^{-1} frequency range. The spectra for pure Gr/Fe@Gly and film formed over mild steel surface by the Gr/Fe@Gly molecules in 1 M HCl after 6 h immersion were obtained. The layer

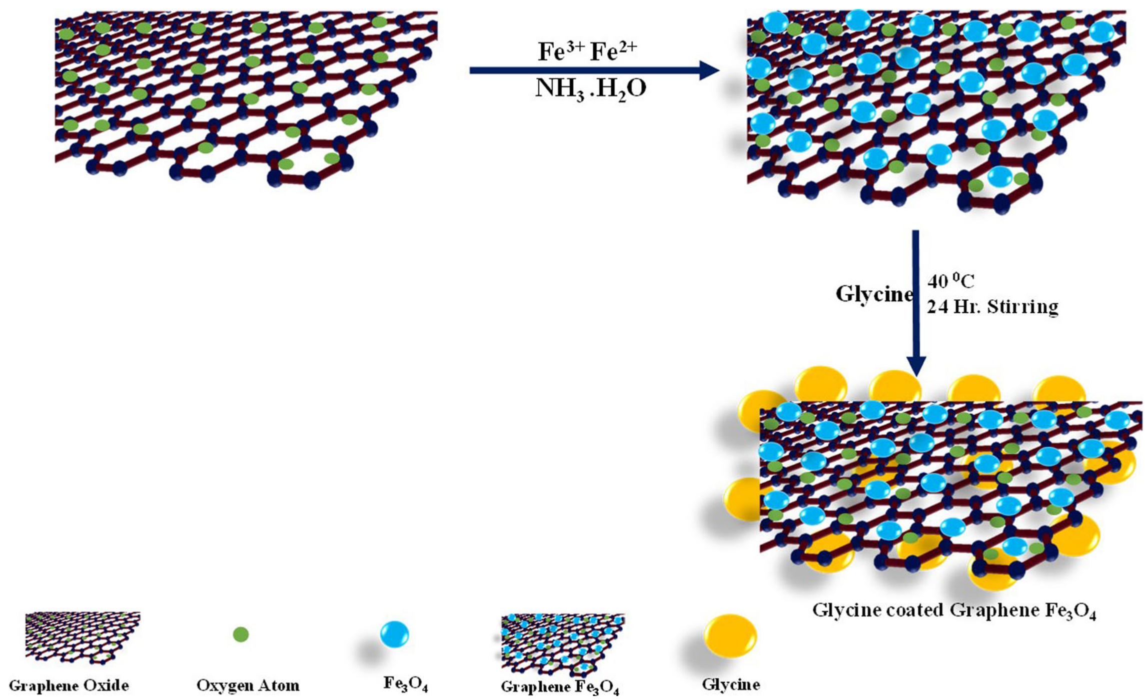

Fig. 1 Synthesis of Gr/Fe@Gly nanocomposite

formed was scrapped, mixed with KBr and then converted to pellets.

2.3.4 SEM Analysis

Using SEM, the effect of nanocomposite-loaded solution on the surface morphology of mild steel was investigated as opposed to the blank solution. For the analysis, the mild steel coupons were prepared as described above. The specimens were collected, adequately washed in acid medium after 6 h of immersion, thoroughly rinsed with distilled water and air-dried and exposed to SEM analysis.

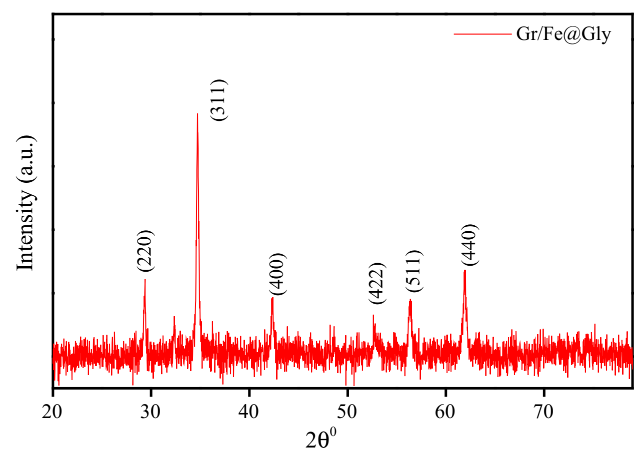

Fig. 2 X-ray diffraction patterns of Gr/Fe@Gly

3 Results and Discussion

3.1 Characterization of Gr/Fe@Gly NC

XRD is utilized to recognize the crystalline structure of the sample. Figure 2 shows the XRD pattern of the Gr/Fe@Gly NC. The diffraction pattern of Gr/Fe@Gly is shown at 2θ angles 30.0, 35.5, 43.1, 53.6, 57.2 and 62.5 matching to crystal planes of (220), (311), (400), (422),(511) and (440), and these can be listed to the face-centered cubic lattice (FCC) crystal structure with JCPDS card no. 19-0629 [31]. It can be noticed that incorporating the reduced graphene oxide sheet has not influenced the crystal structure of Fe_3O_4 NPs. Furthermore, the characteristic peak for reduced graphene oxide sheet is expected at 26° (002), which is very difficult to identify primarily owing to poor intensity contrasted with the dominant Fe_3O_4. It was also observed that the peak positions of the nanocomposite after functionalization with the amino acid, i.e., glycine, did not change. This suggested that after functionalization with glycine, the structure of the core magnetite-reduced graphene oxide remained unchanged.

The average sample size of crystallite (D) was determined according to the Debye-Scherer formula.

$$D = \frac{0.9\lambda}{\beta \cos \theta} \quad (1)$$

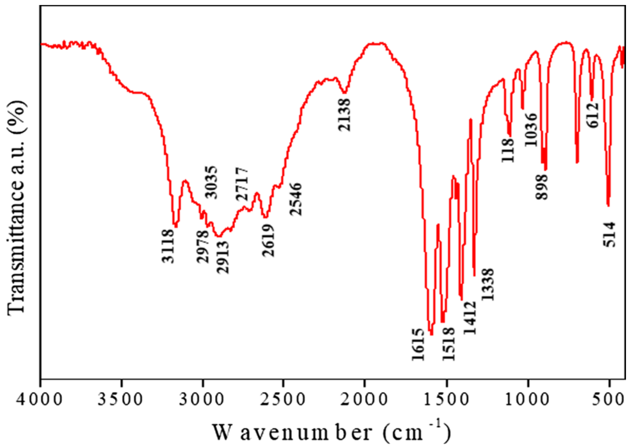

Fig. 3 FT-IR spectra of Gr/Fe@Gly

where $k = 0.9$ is the shape factor, λ is the X-ray wavelength of Cu Kα radiation (1.54 Å), θ is the Bragg diffraction angle and β is the full width of the (311) plane diffraction peak at half maximum height (FWHM). The measured average crystalline size of Gr/Fe@Gly nanocomposite was observed to be 8 nm.

The transition peaks attributable to the carboxylate group (COOH) of glycine are typically found at 607, 1414 and 1605 cm^{-1} [29]. From the FT-IR spectrum of Gr/Fe@Gly NC (Fig. 3), it is clear that the transition peaks attributable to the carboxylate group (COOH) of glycine are shifted to 612, 1412 and 1615 cm^{-1}. The FT-IR peaks mainly because of the ammonium group NH3+ of free glycine were seen at 1133, 1507 and 2614 cm^{-1}, but in the Gr/Fe@Gly NC most of these are shifted to 1126, 1517 and 2619 cm^{-1}, correspondingly [30]. This reflection is evident that the glycine molecule exists in Gr/Fe@Gly as a zwitterionic form. The peaks revealed at 898 and 1338 cm^{-1} are assigned to CCN and CH_2 stretching groups, correspondingly. FT-IR spectra of Gr/Fe@Gly nanocomposite show characteristic peaks for Fe_3O_4 at around 514 cm^{-1} and 470 cm^{-1} are in agreement with the vibration of $Fe_3 + O_2{}^{-}$ complex vibrations in octahedral and tetrahedral sites, correspondingly [31]. The broad absorption spectrum of Gr/Fe@Gly NC, exhibited at 2717 and 2913, corresponds to –O–H stretching vibrations and 2978, 3035 and 3118 cm^{-1} corresponds to N–H stretching vibrations, respectively.

The morphology of the synthesized Gr/Fe@GlyNC was the analyzed with SEM and HR-TEM. Figure 4a–c displays SEM images of Gr/Fe@GlyNC with distinctly wrinkled microstructure on the scale of 1 μm, 0.5 μm and 0.2 μm which was interconnected via a large number of the nanoparticles. Figure 4d shows the EDAX profile which revealed the presence of C, N, O and Fe. Also, Fig. 4d shows elemental mapping assessment which can provide direct elemental distribution of the sample and determine the homogeneous dispersion of carbon (red), nitrogen (green), oxygen (blue) and iron (yellow) atoms in Gr/Fe@GlyNC.

Furthermore, HR-TEM was utilized to determine the functionalization of glycine on graphene/Fe_3O_4 nanoparticle (Fig. 5). At the low magnification TEM images, the surface of the spherical morphology of Fe_3O_4 nanoparticle with the average particle size of 4.8 nm was successfully interacted with flexible graphene sheets and wrapped with glycine which could be observed from Fig. 5a, b. HR-TEM images of Gr/Fe@GlyNC (Fig. 5b, c) were shown black homogeneous dispersion of Fe_3O_4 nanoparticles which embedded on the glycine surface. Figure 5c shows a clearer HR-TEM image of the Fe_3O_4 nanoparticles with the 4.8 diameter distribution. The nature of sample's crystal structure was determined by selected area electron diffraction (SAED) analysis, as shown in Fig. 5d.

Typical SAED pattern for synthesized Gr/Fe@Gly NC suggests a polycrystalline nature (Fig. 5d). The diffraction rings in Fig. 5d correspond well with the (220), (311), (400), (422) and (511) planes of the cubic structure of Fe_3O_4 nanoparticle.

3.2 Weight Loss Study

3.2.1 Effect of Gr/Fe@Gly NC Concentration and Electrolyte Temperature

The results of concentration effect of Gr/Fe@Gly NC and electrolyte temperature on inhibition efficiency, as obtained by weight loss experiments, are given in Table 1. Though the performance of Gr/Fe@Gly NC was moderate at lower temperatures (at 30 °C, maximum efficiency of 78.4% at 50 ppm), it performed more effectively at higher temperatures exhibiting an inhibition efficiency of 94.23% at 60 °C at 5 ppm. The incremental addition of Gr/Fe@Gly NC to the corrosive solution caused further improvement in the inhibition efficacy till it reached an optimum concentration of 50 ppm, the inhibition efficiency being 98.18% at 60 °C. The main reason to explain this event is attributed to increased adsorption of Gr/Fe@Gly NC and more coverage of active sites on the metal surface, causing slowing down of the corrosion process [30]. The Gr/Fe@Gly NC contains –NH_2 and -COOH groups which are likely to undergo protonation and adsorb at the steel surface via electrostatic attraction or via forming bridges with the Fe^{2+} ions. The GO moieties were supposed to provide efficient metal surface coverage that could reduce the surface area suitable for corrosive acid electrolyte attack. On the other hand, the presence of numerous lone pair electrons onto the structure of Gr/Fe@Gly NC and also a great number of vacant orbitals of iron metal provide a condition causing the creation of the chelated compound.

The improved performance of Gr/Fe@Gly NC at higher temperatures could be assigned to a change in adsorption

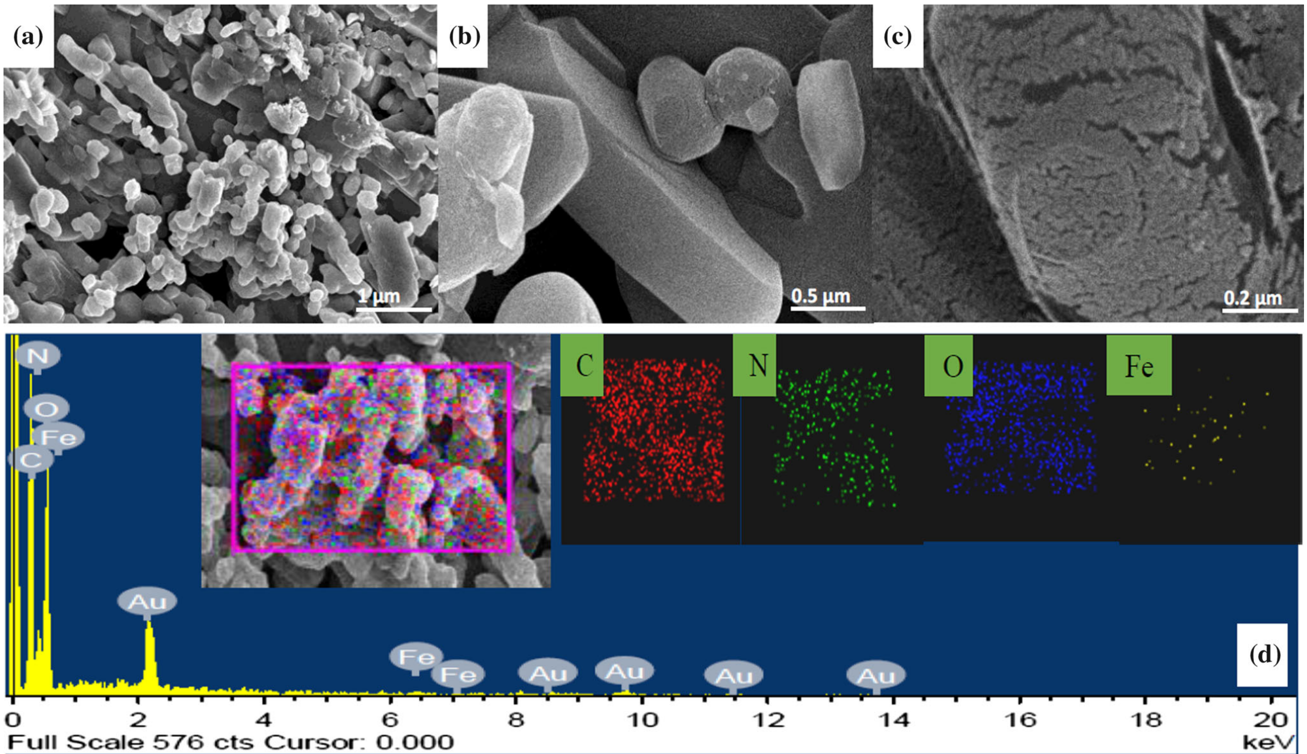

Fig. 4 SEM micrograph of Gr/Fe@Gly **a** 1 µm scale, **b** 0.5 µm scale, **c** 0.2 µm scale, **d** EDX and mapping

Table 1 Corrosion parameters of mild steel following 6 h immersion in 1 M HCl solution in the absence and presence of different concentrations of Gr/Fe@Gly NC at different temperatures

C (ppm)	30 °C		40 °C		50 °C		60 °C		70 °C	
	υ (mg cm^{-2} h^{-1})	η (%)	υ (mg cm^{-2} h^{-1})	η (%)	υ (mg cm^{-2} h^{-1})	η (%)	υ (mg cm^{-2} h^{-1})	η (%)	υ (mg cm^{-2} h^{-1})	η (%)
0	0.130 ± 0.001	–	0.380 ± 0.001	–	2.204 ± 0.015	–	3.51 ± 0.040	–	4.48 ± 0.045	–
1	0.048 ± 0.001	63.1	0.114 ± 0.001	70.0	0.273 ± 0.003	87.6	0.41 ± 0.010	88.30	1.59 ± 0.013	64.40
5	0.042 ± 0.001	67.3	0.082 ± 0.001	78.4	0.140 ± 0.002	93.6	0.20 ± 0.010	94.23	1.28 ± 0.011	71.33
10	0.037 ± 0.001	71.3	0.061 ± 0.001	84.0	0.082 ± 0.002	96.3	0.10 ± 0.003	97.09	1.19 ± 0.011	73.42
50	0.028 ± 0.001	78.4	0.043 ± 0.001	88.8	0.045 ± 0.001	97.9	0.06 ± 0.001	98.18	1.09 ± 0.023	75.55
100	0.039 ± 0.001	69.3	0.068 ± 0.001	82.0	0.284 ± 0.005	87.1	0.28 ± 0.010	91.89	0.28 ± 0.010	93.66
300	0.048 ± 0.001	62.6	0.082 ± 0.001	78.4	0.362 ± 0.001	83.6	0.36 ± 0.010	89.68	0.36 ± 0.010	91.93
500	0.049 ± 0.001	61.9	0.083 ± 0.001	78.0	0.368 ± 0.006	83.3	0.37 ± 0.010	89.51	0.37 ± 0.010	91.79

"±" shows the standard deviation of three measurements

mode from dominantly physical nature at lower temperature to chemical nature as temperature is increased. The increase in electrolyte temperature resulted in enhanced desorption of water molecules from metal surface and hence increased availability of surface area for adsorption of Gr/Fe@Gly NC. Moreover, at high temperature, glycine may play the role of a catalyst and thereby facilitate the reduction of GO. During the reduction process, a new bond C-N may arises due to ring opening of the epoxy group of GO [18] which may be responsible for the enhanced adsorption capacity of NC.

Further, as per the results presented in Table 1 after a specific inhibitor quantity, i.e., 50 ppm, an increment of inhibitor dosage in solution results in decrease in protection efficacies (62.6% at 300 ppm) which in turn became almost constant (61.9% at 500 ppm); this may be related to the fact that the inhibitor molecules couldn't adsorb on steel substrate due to unavailability of active sites for adsorption. However, corrosion still occurred which means the inhibitive layer didn't change but corrosion activity increased. So, for this reason the inhibition performance decreased to lower values. Further, when the steel sites are fully covered, an

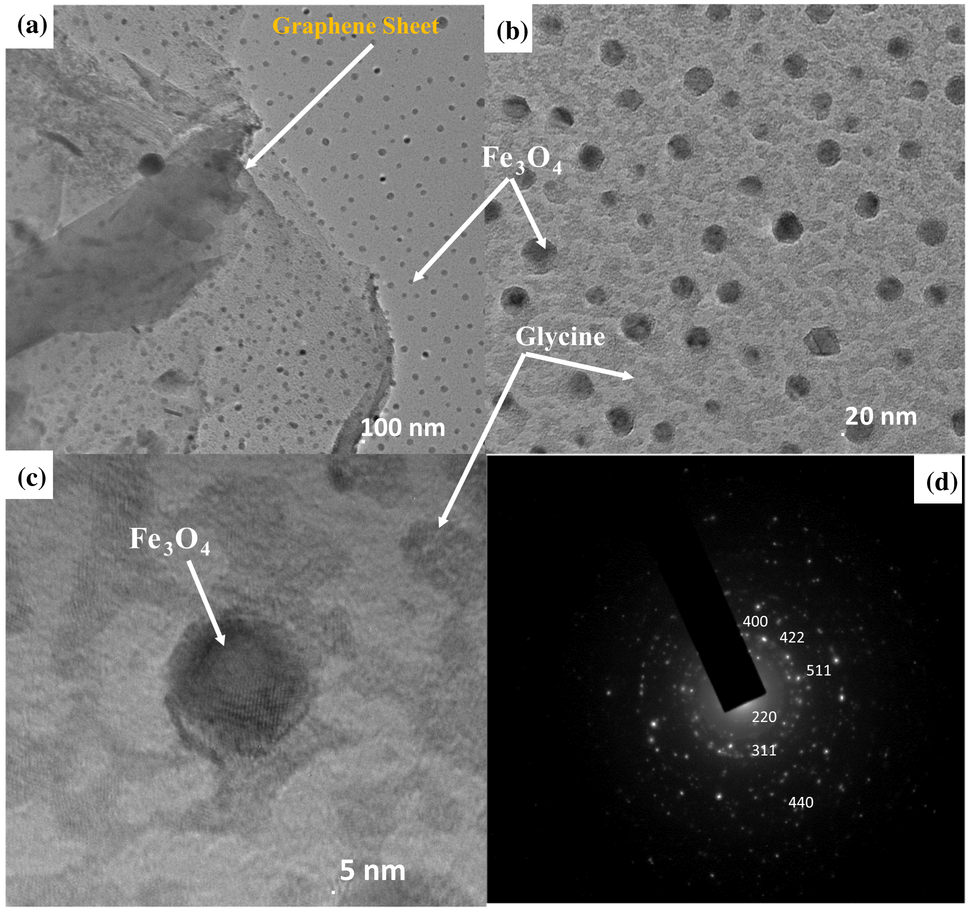

Fig. 5 TEM micrograph of Gr/Fe@Gly **a** 100 nm scale, **b** 20 nm scale, **c** 5 nm scale, **d** SAED pattern

increment of inhibitor concentration did not change the efficiency. So, in the present study the 50 ppm can be considered as the optimal threshold of the inhibitor. The decrease in inhibition efficiency above 60 °C is due to shift in the adsorption–desorption equilibrium toward desorption of the inhibitor molecules.

3.2.2 Activation Parameters

The activation energy (E_a) for metallic corrosion is the minimum amount of energy needed to produce the corrosion product. The natural logarithm of corrosion rate (ν) behaves as linear function with $1/T$ (Fig. 6a). Thus, the E_a value could be obtained by measuring the linear slope ($-E_a/R$) of Eq. (4).

$$\log \nu = \log A - \frac{E_a}{2.303RT} \quad (2)$$

where A is a pre-exponential constant of Arrhenius, R is a constant of molar gas (8.314 J K^{-1} mol^{-1}) and T is the absolute temperature.

It is evident from Table 2 that the E_a values of inhibited systems are smaller than those of the uninhibited ones, and a decrease in E_a is noted with an increase in concentration

Table 2 Activation parameters of adsorption for MS in 1 M HCl at different temperatures

C (ppm)	E_a	ΔH^*_{ads} (KJ mol^{-1})	ΔS^*_{ads} (KJ mol^{-1})
0	97.37	95.49	0.110
1	61.37	59.49	− 0.015
5	43.71	41.83	− 0.075
10	27.89	26.02	− 0.128
50	21.26	19.38	− 0.127

of Gr/Fe@Gly NC. Similar results were published in the literature [12, 32] and were interpreted as chemical adsorption indicatives. By using an alternative form of Arrhenius equation, activation enthalpy (ΔH^*) and activation entropy (ΔS^*) were computed [30].

$$\nu = \frac{RT}{Nh}\exp\left(\frac{\Delta S*}{R}\right)\exp\left(-\frac{\Delta H*}{RT}\right) \quad (3)$$

where N is the Avogadro number and h is the Planck's constant.

By the slope ($-\Delta H^*/2.303R$) and intercept [$\log(R/Nh) + (\Delta S^*/2.303R)$] (Fig. 6b) of Eq. (8), the values of ΔH^* and

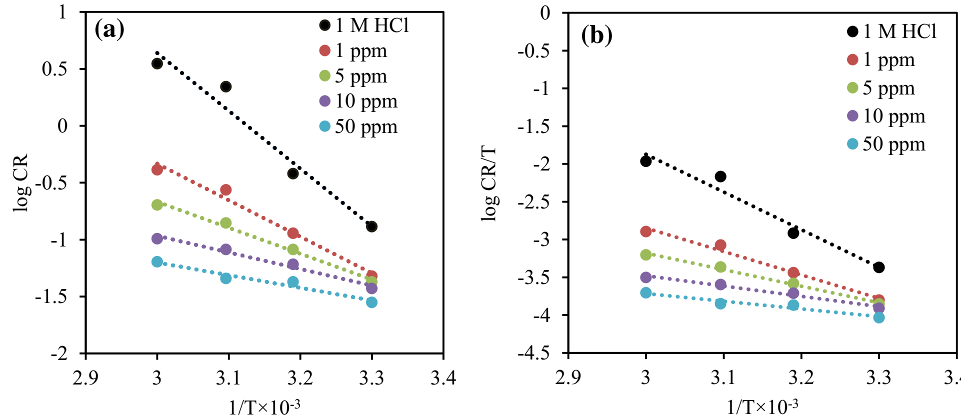

Fig. 6 **a** Arrhenius, **b** alternative Arrhenius plots for MS in 1 M HCl in the absence and presence of different concentrations of Gr/Fe@Gly NC

ΔS^*, were determined correspondingly. The positive values shown in Table 2 showed the endothermic aspect of the activated step for the process of metallic dissolution. In addition, the value for the dissolution of steel surfaces in acid solution containing 50 ppm Gr/Fe@Gly NC is lower (23.14 kJ mol^{-1}) than that for its absence (112.25 kJ mol^{-1}), indicating a slow rate of dissolution of steel surfaces in the presence of NC [32]. Furthermore, the ΔS^* negative values indicate that the activated complex in the rate determination step is an association rather than a dissociation step [33, 34]. Comparison of the entropy of activation values in both inhibited and uninhibited acid media shows that ΔS^* values are lower (−0.140 J mol^{-1} K^{-1}) for a solution inhibited by 10 ppm Gr/Fe@Gly NC than for an uninhibited solution (−0.164 J mol^{-1} K^{-1}) likely to be due to an improvement of solvent entropy (H_2O) resulting from H_2O desorption from a mild steel surface in the presence of Gr/Fe@Gly [12].

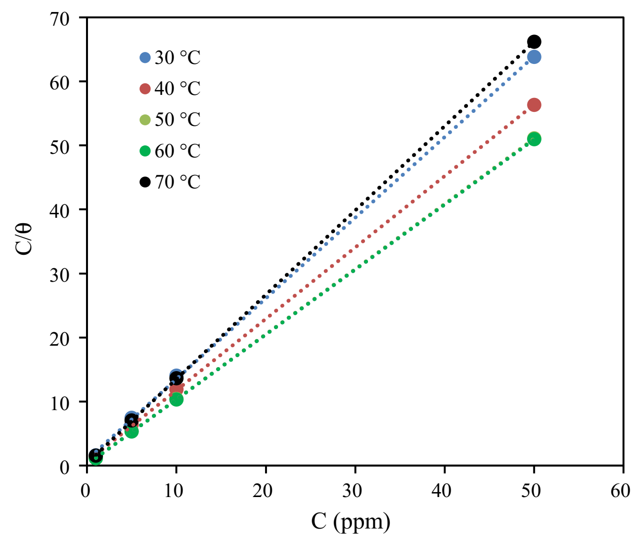

Fig. 7 Langmuir adsorption isotherm for Gr/Fe@Gly NC adsorbed on the MS surface in 1 M HCl solution at different temperatures

3.2.3 Adsorption Isotherm and Thermodynamic Parameters

The fitting of the surface coverage data (θ), evaluated from weight loss studies, was achieved with different isotherm adsorption models, and the best match for the Langmuir isotherm, defined as Eq. (6), was presented. In this equation, concentration is C, and adsorption equilibrium constant is presented as K_{ads}.

$$\frac{C}{\theta} = \frac{1}{K_{ads}} + C \tag{4}$$

The fitting of the Langmuir adsorption isotherm was very good, with a correlation factor (R^2) and slope value close to unity. This indicates that, according to a Langmuir adsorption isotherm, the inhibitor molecules were adsorbed to the mild steel surface, indicating the absence of interaction forces among adsorbed molecules. The K_{ads} values were determined from the intercepts of the straight lines of C versus C/θ-axis (Fig. 7) and displayed in Table 3. The value of K_{ads} is an indicator that studied inhibitor molecules interact better and stronger on the metal surface [35].

Furthermore, it is also important to discuss the values of standard free energy of adsorption ($\Delta G°_{ads}$) given in Table 3, which is linked to K_{ads} with the following equation:

$$\Delta G^{\circ}_{ads} = -RT\ln\left(10^6 K_{ads}\right) \tag{5}$$

where the factor 10^6 reflects the amount (in ppm) of water molecules, the negative values of $\Delta G°_{ads}$, support the spontaneous adsorption of Gr/Fe@Gly NC molecules on the metal surface [36, 37].

The Van't Hoff equation (Eq. 8) and Fig. 8 finds the standard adsorption enthalpy ($\Delta H°_{ads}$):

$$\log K_{ads} = \frac{-\Delta H^{\circ}_{ads}}{2.303RT} + \text{constant} \tag{6}$$

Table 3 Thermodynamic parameters of adsorption for MS in 1 M HCl at different temperatures

Temp (°C)	K_{ads} (L ppm^{-1})	$\Delta G°_{ads}$ (KJ mol^{-1})	$\Delta H°_{ads}$ (KJ mol^{-1})	$\Delta S°_{ads}$ (KJ mol^{-1})
30	1.07	– 34.99	53.04	– 0.290
40	1.64	– 37.23		– 0.118
50	5.17	– 41.51		– 0.128
60	6.12	– 43.26		– 0.129

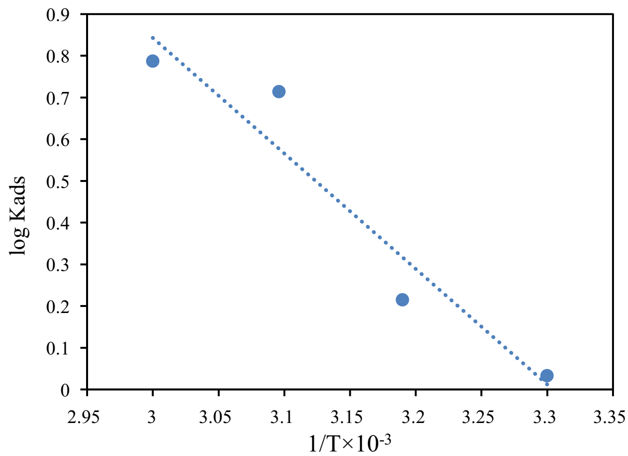

Fig. 8 Plot of log K_{ads} versus 1/T of Gr/Fe@Gly NC

where – $\Delta H°_{ads}/2.303RT$ is the slope of the straight line of the plot between log K_{ads} and 1/T. The values of the standard entropy of adsorption ($\Delta S°_{ads}$) were obtained from Eq. (7):

$$\Delta G^{\circ}_{ads} = \Delta H^{\circ}_{ads} - T\Delta S^{\circ}_{ads} \tag{7}$$

The value of the $\Delta H°_{ads}$ provides information about the inhibitor adsorption mechanism. $\Delta H°_{ads} > 0$ reflects chemical adsorption for an endothermic adsorption process, whereas $\Delta H°_{ads} < 0$ reflects physical adsorption [38, 39]. In this survey, the positive value of $\Delta H°_{ads}$ implies endothermic adsorption. Related findings were published by Hoseinzadeh et al. [40] and Solomon et al. [41]. As is evident from Table 3, $\Delta H°_{ads}$ value exceeds zero and hence verifies the process of chemical adsorption indicated by the variation of η with temperature. The calculated positive value of – $\Delta S°_{ads}$ was correlated with the increase in solvent energy and a higher positive desorption entropy of H_2O [41]. This may also be linked to the replacement of more water molecules over the metal surface by one inhibitor molecule.

3.3 EIS Study

The Nyquist and Bode (impedance and phase angle) plots for mild steel corrosion in 1 M HCl in the absence and presence of Gr/Fe@Gly NC at 30 °C are demonstrated in Fig. 9a–c, and the associated data are listed in Table 4. The shape of Nyquist diagrams (Fig. 9a) appears in a single semicircular form; it is inferred that the system response (substrate/solution interface) must contribute to the charge transfer process. In addition, although increasing inhibitor concentration, no noticeable change in the shape of Nyquist spectra is observed.

This may prove true that the occurrence of corrosion is under charge transfer control. Nevertheless, the absence of perfect surface homogeneity leads to no exact semicircle curves. A constant phase element (CPE) in place of pure capacitance is introduced in the equivalent circuit to overcome this situation (Fig. 9d). The CPE is defined as impedance values as indicated in Eq. (8):

$$Z_{CPE} = \frac{1}{Y_o(j\omega)^n} \tag{8}$$

whereY_o: represents the magnitude of CPE;ω: represents the angular frequency in Rads^{-1} ($\omega = 2\pi f_{max}$, f_{max} is the frequency); j represents the imaginary unit; and n represents the phase shift (exponent) representing surface irregularities. The CPE is classifiable by the n values as follows: CPE represents resistance ($n = 0$, $Y_o = R$), capacitance ($n = 1$, $Y_o = C$), inductance ($n = -1$, $Y_o = L^{-1}$) and Warburg impedance ($n = 0.5$, $Yo = W$) [42]. The fitting of the spectrum to the equivalent circuit model allows the development of the elements of the circuit analogue in which constant phase element and the polarization resistance is in parallel combination and these two are connected to the electrolyte resistance (R_s) in series. The experimental and computer fit results of the Nyquist plot of 1 M HCl containing various dosages at 30 °C are demonstrated in Fig. 9. Low χ^2 (Chi-square) values listed in Table 4 indicate the fitness of the EIS plots and thus validate the selection of the equivalent circuit. Moreover, the capacitance of double layer (C_{dl}) is determined using CPE parameters, i.e., n and Y_o, by the equation followed [43]:

$$C_{dl} = Y_0(2\pi f_{max})^{n-1} \tag{9}$$

Inhibition efficiencies were calculated using the following formula from polarization resistance:

$$\eta_R(\%) = \frac{R_p^{(i)} - R_p^{(0)}}{R_p^{(i)}} \times 100 \tag{10}$$

where $Rp^{(0)}$ [sum of the charge transfer resistance (R_{ct}), diffuse layer resistance (R_d) and accumulation resistance (R_a)]

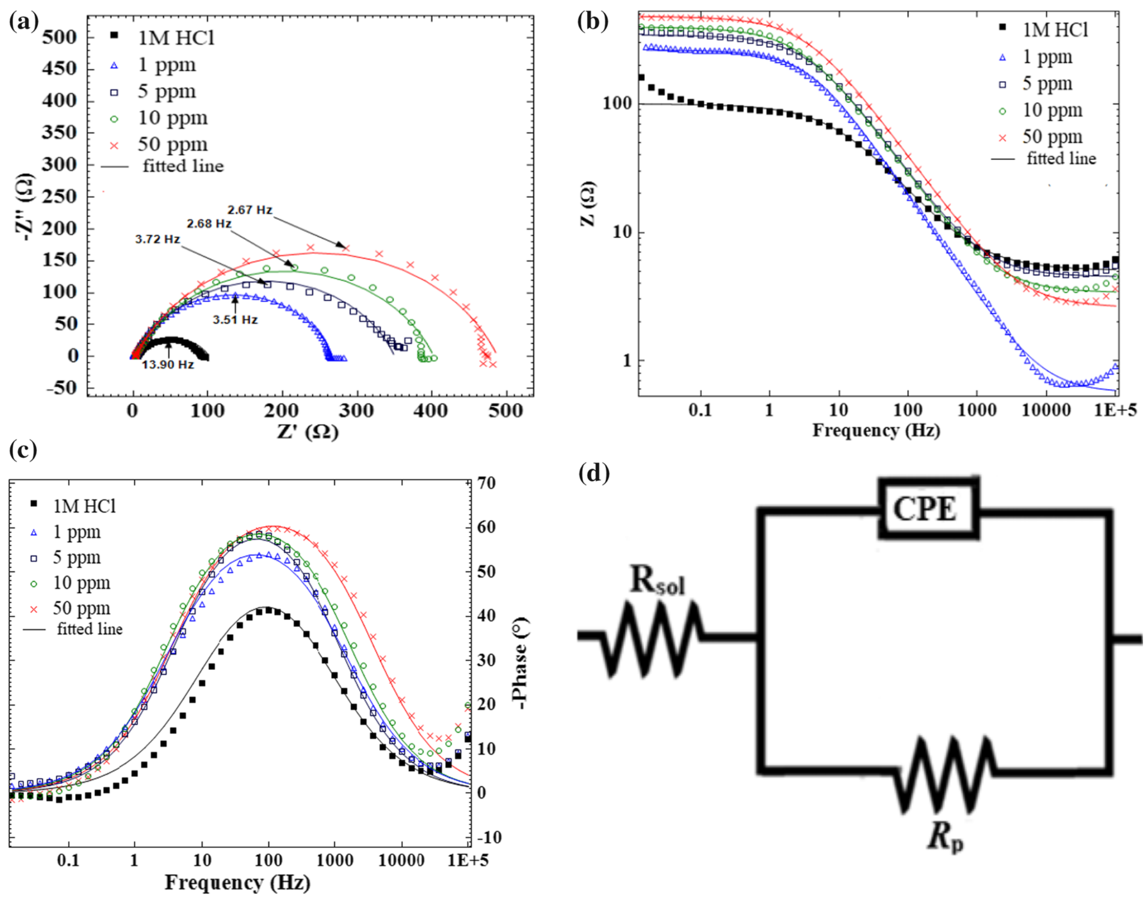

Fig. 9 **a** Nyquist, **b** Bode impedance, **c** Bode phase angle plots for mild steel in 1 M HCl solution without and with various dosages of Gr/Fe@Gly NC and **d** equivalent circuit used to fit EIS spectra

Table 4 Electrochemical parameters for mild steel at 30 °C in 1 M HCl solution in the presence and absence of different concentrations of Gr/Fe@Gly NC

C (ppm)	R_s (Ω cm^2)	R_p (Ω cm^2)	$C_{dl} \times 10^{-4}$ (F cm^{-2})	$\chi^2 \times 10^{-4}$	$-S$	$-\theta$	η_{EIS} (%)
0	4.64 ± 0.02	91.7 ± 0.9	1.52 ± 0.01	3.4	0.479	41.28	–
1	4.40 ± 0.03	266.7 ± 3.1	1.47 ± 0.01	4.1	0.521	53.21	65.6
5	4.18 ± 0.04	345.0 ± 7.0	1.26 ± 0.01	2.8	0.652	58.06	71.6
10	3.36 ± 0.01	387.1 ± 5.2	1.19 ± 0.01	3.9	0.663	58.48	76.8
50	2.44 ± 0.01	427.0 ± 7.4	1.16 ± 0.01	1.2	0.673	59.75	78.5

"±" shows the standard deviation of three measurements

and $Rp^{(i)}$ [sum of the R_{ct}, R_d, R_a and film resistances (R_f)] [44] are the polarization resistances of mild steel without and with the inhibitor, respectively.

The increase in R_p values, and consequently an increase in inhibition efficiency, with incremental addition of Gr/Fe@Gly NC can be attributed to the gradual replacement of water molecules by the adsorption of the inhibitor molecules on the metal surface to create an adherent film. The present study shows the highest value of R_p (426.9 Ω cm^2) at 50 ppm with corresponding inhibition efficiency of 78.5%. The resulting decrease in C_{dl} values with the addition of Gr/Fe@Gly NC is due to an increase in the thickness of the electronic double layer/decrease in the local dielectric constant, suggesting that at both anodic and cathodic sites of the mild steel surface, nanocomposite molecules were adsorbed [45].

In the obtained Bode impedance plot (log Z vs. log f plot, Fig. 9b), the impedance values increase with adding inhibitor dosage, suggesting the rate of corrosion decreases in the presence of inhibitor. According to the single wave phase angle–frequency curves (phase angle vs. log f, Fig. 9c), only one time constant ensures that the charge transfer process consists of single relaxation process. On adding the inhibitor, broadening in the Bode plots occurs due to the adsorption

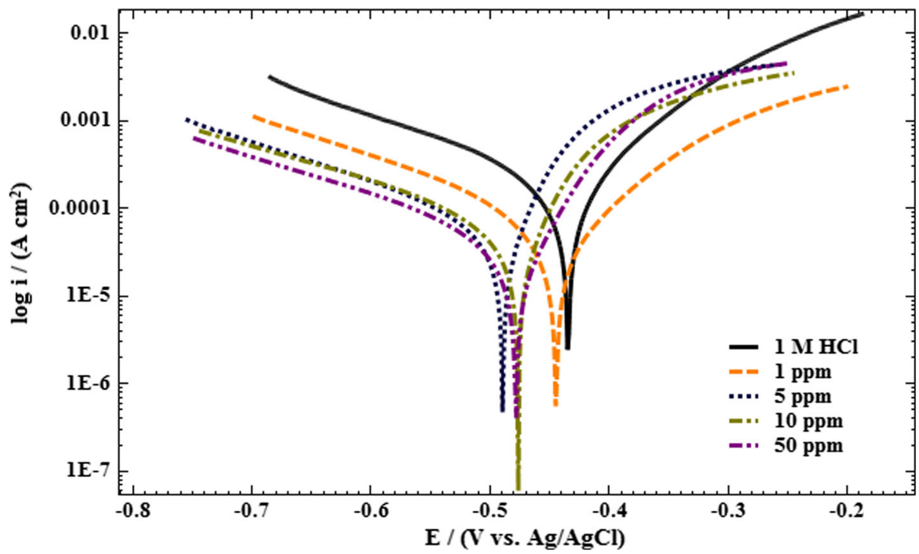

Fig. 10 PDP plots for mild steel in 1 M HCl solution without and with various dosages of Gr/Fe@Gly NC

Table 5 Potentiodynamic polarization parameters for mild steel at 30 °C in 1 M HCl solution in the presence and absence of different concentrations of Gr/Fe@Gly NC

C (ppm)	E_{corr} (V vs. Ag/AgCl)	β_a (V dec^{-1})	$-\beta_c$ (V dec^{-1})	$I_{corr} \times 10^{-4}$(A cm^{-2})	η_{PP} (%)
0	-0.434 ± 0.003	0.103 ± 0.001	0.068 ± 0.001	1.03 ± 0.003	–
1	-0.446 ± 0.008	0.106 ± 0.001	0.098 ± 0.001	0.39 ± 0.002	61.7
5	-0.487 ± 0.007	0.103 ± 0.001	0.042 ± 0.001	0.33 ± 0.006	67.9
10	-0.476 ± 0.002	0.092 ± 0.001	0.045 ± 0.001	0.28 ± 0.003	72.9
50	-0.477 ± 0.005	0.108 ± 0.001	0.060 ± 0.001	0.23 ± 0.001	78.2

"±" shows the standard deviation of three measurements

of inhibitor molecules. At intermediate frequency, the phase angle value is $-41.28°$ in the absence of inhibitor and this value in the presence of optimum concentration of inhibitor is $-59.75°$. An increase in phase angle value approaching to 90° indicates capacitive electrochemical behavior of the steel solution interface [46].

3.4 PDP Study

Aiming to extend the results of EIS and to provide more informative findings on corrosion inhibition behavior of synthesized NC, PDP study was carried out further. The impact of the concentration of the investigated NC on the polarization character of mild steel in 1 M HCl at 30 °C was analyzed, and the curves were recorded for the various concentrations of inhibitor (Fig. 10). On the other hand, various polarization parameters are given in Table 5 including the corrosion potential (E_{corr}), anodic (β_a) and cathodic (β_c) Tafel slopes, corrosion current density (I_{corr}), deduced from curves, and the percent inhibition efficacies (η_{PP}) calculated from I_{corr}. According to the Tafel curves obtained and the results of Table 5, it is seen that the E_{corr} moves toward the more negative potentials with the different concentrations of the NC. Moreover, the Tafel curves demonstrate the lowering of current density of the cathodic (β_c) extension in the presence of NC relative to the blank. Following the corrosion potential and current density displacements, we can conclude that the studied NC is classified as cathodic inhibitor type [47]. The values of I_{corr} significantly diminished in the presence of NC in 1 M HCl solution. The presence of 1 ppm NC reduced the I_{corr} from 1.03×10^{-4}(A cm^{-2}) (blank) to 0.39×10^{-4} (A cm^{-2}), and this corresponds to inhibition efficiency of 61.7%. At optimum concentration (50 ppm), I_{corr} attained the lowest values of 0.23×10^{-4} (A cm^{-2}) and the metal surface was protected by 78.2%. The inhibition efficiency values increased with rising concentration of inhibitor, indicating the inhibitory effect of NC to corrosion of mild steel in the studied corrosive environment.

In order to establish the cost-effectiveness and practical applicability of Gr/Fe@Gly NC, the inhibition performance offered by Gr/Fe@Gly NC at optimum concentration was compared with the previously studied glycine, glycine derivatives and magnetite nanoparticles [48, 8, 49–57]. The results given in Table 6 exhibited the superiority of the Gr/Fe@Gly NC as corrosion inhibitor over glycine, glycine derivatives and magnetite nanoparticles at very low dosage making it more practical and economically viable inhibitor.

3.5 Statistical Analysis

ANOVA was used for statistical analysis at 95%confidence level, i.e., at significance level (α) of 0.05, and the result is

Table 6 Comparison of the inhibition performance of investigated Gr/Fe@Gly NC with glycine, its derivatives and magnetite nanoparticle used for the inhibition of mild steel corrosion

S. no.	Inhibitor	C (ppm)	Medium	IE (%)	Reference
1.	Glycine	75	0.1 M HCl	40.3	[48]
2.	Glycine	75	1 M HCl	1.6	[49]
3	Glycine	75	4.0 M H_2SO_4	14.0	[50]
4.	Glycine	100		50.1	[51]
5.	2-(4-(Dimethylamino)benzylamino)acetic acid hydrochloride (GlyD1)	97	4.0 M H_2SO_4	20.0	[52]
6.	*N*,*N*-bis(2-aminoethyl)glycine (GlyD2)	138	4.0 M H_2SO_4	6.2	[52]
7.	Glycine derivative *N*-benzylidine-2((2-oxo-2-(10Hphenothiazine-10yl)ethyl)amino) acetohydrazide	50	1 M HCl	70.0	[53]
8.	Myrrh +magnetite nanoparticle	50	1 M HCl	74.3	[8]
9.	Magnetite-RK/amidoxime nanoparticle	50	1 M HCl	80.4	[54]
10.	Fe_3O_4/poly(2-acrylamido-2-methylpropane sulfonic acid) (PAMPS) magnetic nanogels	50	1 M HCl	59.73	[55]
11.	PAni-PAAm/Fe_3O_4	80	1 M HCl	78	[56]
12.	2-Acrylamido-2-methylpropane sulfonic acid (AMPS) magnetite nanogel	50	1 M HCl	50.0	[57]
13.	2-Acrylamido-2-methylpropane acrylic acid (AA)magnetite nanogel	50	1 M HCl	56.3	[57]
14.	2-Acrylamido-2-methylpropane acrylamide (AM) magnetite nanogel	50	1 M HCl	69.7	[57]
15.	Gr/Fe@Gly NC	50	1 M HCl	78.4	Present study

Table 7 Analysis of variance (ANOVA) for inhibition efficiency of Gr/Fe@Gly NC using different techniques (WL, PDP and EIS) in 1 M HCl

	Degree of freedom	Sum of squares	Mean square	*F* value	*P* value
Between techniques	1	19.22	19.22	0.504	0.504
Residual	6	228.49	38.08		
Total	7	247.72			

given in Table 7. From this table, the *p* value of the ANOVA is 0.504, which is greater than α. From *p* value, it is assumed that there is no statistically significant difference between the inhibition efficiencies obtained by different techniques such as gravimetric, PDP and EIS.

3.6 FT-IR Study

To further verify the adsorption of Gr/Fe@Gly NC molecules on mild steel surface in 1 M HCl solution, the FT-IR analysis of the film extracted from mild steel sample immersed in 1 M HCl solution containing 50 ppm of Gr/Fe@Gly NC for 6 hat 30 °C was recorded.

The prominent functional groups identified in the spectrum of Gr/Fe@Gly NC included C–H stretch at 2894 cm^{-1}, O–H at 2717, 2913 cm^{-1}, C=O stretch at 1615 cm^{-1}, C–H rocking vibration at 1338 cm^{-1}, C–N stretch at 1121 cm^{-1}, C–O stretch at 1072 cm^{-1} and CCN at 898 cm^{-1}. The obtained spectrum is compared with the FT-IR spectrum of film formed by Gr/Fe@Gly NC extracted from mild steel sample (Fig. 11). It could be seen in Fig. 11 that the two spectra are similar; however, some functional groups were shifted to lower wavenumber/intensity. The peak arising from COOH at 1412 and 1615 cm^{-1} and OH stretching at 2717 and

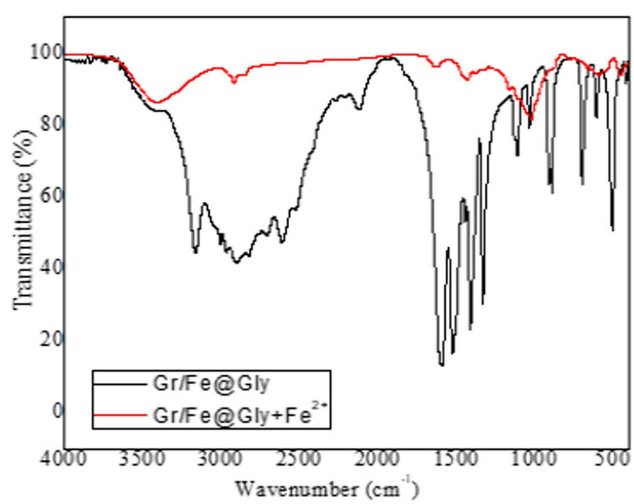

Fig. 11 FT-IR adsorption spectrum for pure Gr/Fe@Gly NC and adsorbed film (Fe–Gr/Fe@Gly NC) on the MS surface

2913 cm^{-1} in the NC spectra shifted to 1427 and 1625 cm^{-1} and 2796 and 2927 cm^{-1} in the film spectrum. It represents the role of oxygen heteroatom in the process of adsorption. More shift in FT-IR absorption band frequency indicates the

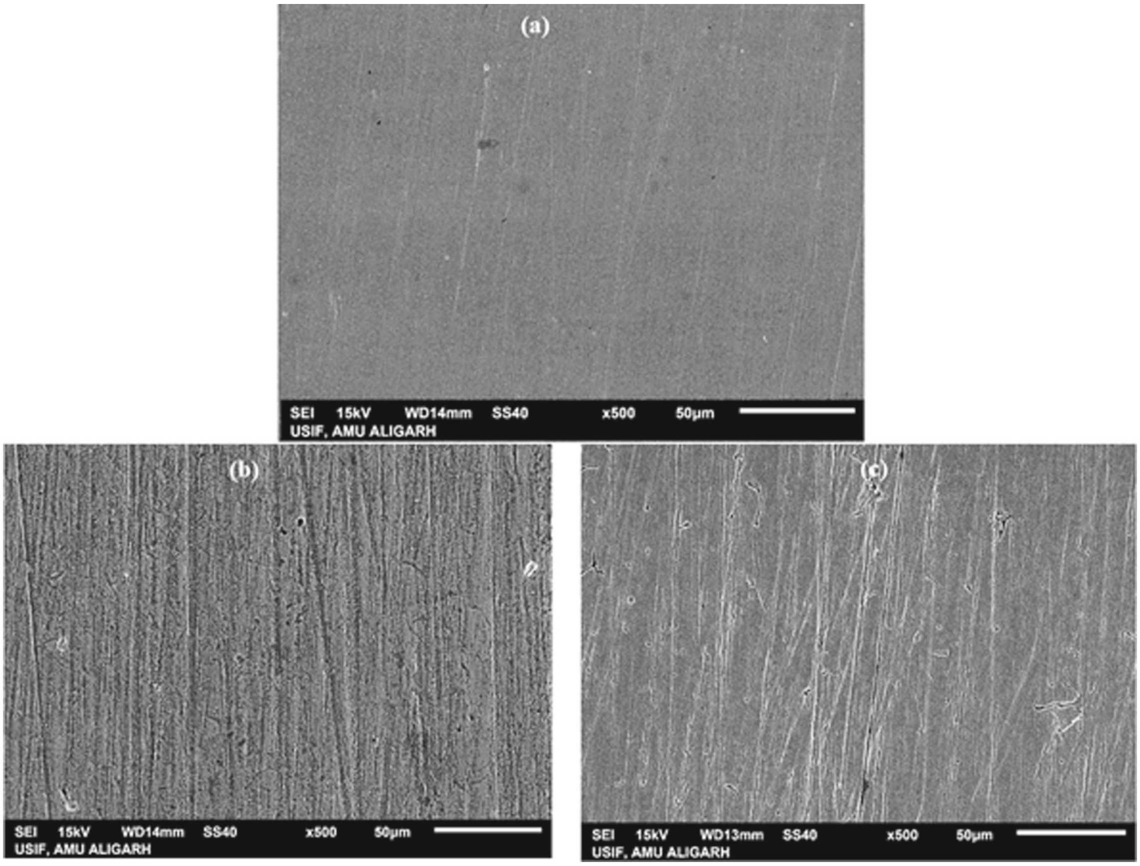

Fig. 12 SEM photomicrographs: **a** polished mild steel surface, **b** mild steel surface immersed in uninhibited acid, **c** mild steel surface immersed in 50 ppm Gr/Fe@Gly NC inhibited acid

interaction between the inhibitor and the metal surface in question.

3.7 SEM Study

SEM study has widely been used to examine the effectiveness of inhibitors on reducing the corrosion process on metallic surfaces. SEM micrographs appear in Fig. 12a–c, where mild steel specimens are immersed in 1 M HCl solution with and without inhibitor for a length of 6 h. As shown in Fig. 12a, the freshly polished mild steel surface was smooth and non-corroded with few polishing scratches. Figure 12b shows that the steel surface was damaged after immersion in an uninhibited solution as a result of rapid corrosion attack on metal by an acid media. However, it is clearly noticed that (Fig. 12c) the rough and corroded steel surface displaces much better and smoother surface in the presence of Gr/Fe@Gly NC inhibitor. This comes from the formation of protective film over the mild steel surface responsible for inhibiting corrosion.

4 Conclusion

The study on the performance of Gr/Fe@Gly NC as mild steel corrosion inhibitor in acidic condition was done successfully. Gr/Fe@Gly NC depicted its effectiveness and stability up to 60 °C at optimum concentration of 50 ppm the inhibition efficiency being 98.28%. Adsorption isotherm study reveals that inhibitor obeyed Langmuir isotherm and inclined more to chemical adsorption. FT-IR analysis confirmed the presence of active functional groups which is responsible for the mild steel inhibition in acidic medium. Overall, the finding of this study suggests that Gr/Fe@Gly NC is preferable due to its long-lastingness and strong adsorption to be used as a mild steel corrosion inhibitor in 1 M HCl medium.

Acknowledgements Ruby Aslam gratefully acknowledges Council of Scientific and Industrial Research (CSIR), New Delhi, India, for Research Associate fellowship (File Number 09/112(0616)2K19 EMR-I). Thanks are also due to University Sophisticated Instrument Facility (USIF), A.M.U. Aligarh, India, for providing TEM, SEM and EDS facility.

Compliance with Ethical Standards

Conflict of interest The authors wish to state that no conflict of interest exists with this manuscript.

References

1. Dutta, D.; Ganda, A.N.F.; Chih, J.K.; Huang, C.; Tseng, C.J.; Su, C.Y.: Revisiting graphene-polymer nanocomposite for enhancing anti-corrosion performance: a new insight into interface chemistry and diffusion model. Nanoscale **10**, 12612–12624 (2018)
2. Mosa, J.; Rosero-Navarro, N.C.; Aparicio, M.: Active corrosion inhibition of mild steel by environmentally-friendly Ce-doped organic–inorganic sol–gel coatings. RSC Adv. **6**, 39577–39586 (2016)
3. Mazumder, M.A.J.: Synthesis, characterization and electrochemical analysis of cysteine modified polymers for corrosion inhibition of mild steel in aqueous 1 M HCl. RSC Adv. **9**, 4277–4294 (2019)
4. Murayama, M.; Nishimura, T.; Tsuzaki, K.: Nano-scale chemical analysis of rust on a 2% Si-bearing low alloy steel exposed in a coastal environment. Corros. Sci. **50**, 2159–2165 (2008)
5. Nalwa, H.S.: Handbook of Nanostructured Materials and Nanotechnology, vol. 1, p. 75. Academic Press, San Diego (2000)
6. Alam, J.; Riaz, U.; Ashraf, S.M.; Ahmad, S.: Corrosion-protective performance of nano polyaniline/ferrite dispersed alkyd coatings. J. Coat. Technol. Res. **5**, 123–128 (2007)
7. Solomon, M.M.; Gerengi, H.; Kaya, T.; Umoren, S.A.: Performance evaluation of a chitosan/silver nanoparticles composite on St37 steel corrosion in a 15% HCl solution. ACS Sustain. Chem. Eng. **5**, 809–820 (2017)
8. Atta, A.M.; Mahdy, G.A.; Al-Lohedan, H.A.; Al-Hussa, S.A.: Corrosion inhibition of mild steel in acidic medium by magnetite myrrh nanocomposite. Int. J. Electrochem. Sci. **9**, 8446–8457 (2014)
9. Stankovich, S.; Dikin, D.A.; Dommett, G.H.; Kohlhaas, K.M.; Zimney, E.J.; Stach, E.A.; Piner, R.D.; Nguyen, S.T.; Ruoff, R.S.: Graphene-based composite materials. Nature **442**, 282–286 (2006)
10. Nine, M.J.; Cole, M.A.; Trana, D.N.H.; Losic, D.: Graphene: a multipurpose material for protective coatings. J. Mater. Chem. A **3**, 12580–12602 (2015)
11. Zhu, Y.W.; Murali, S.; Cai, W.W.; Li, X.S.; Suk, J.W.; Jeffrey, R.P.; Rodney, S.R.: Graphene and graphene oxide: synthesis, properties, and applications. Adv. Mater. **22**, 3906–3924 (2010)
12. Ansari, K.R.; Chauhan, D.S.; Quraishi, M.A.; Saleh, T.A.: Bis(2-aminoethyl)amine-modified graphene oxide nanoemulsion for carbon steel protection in 15% HCl: effect of temperature and synergism with iodide ions. J. Colloid Interface Sci. **564**, 124–133 (2020)
13. Ansari, K.R.; Chauhan, D.S.; Quraishi, M.A.; Adesin, A.Y.; Saleh, T.A.: The synergistic influence of polyethyleneimine grafted graphene oxide and iodide for the protection of steel in acidizing conditions. RSC Adv. **10**, 17739–17751 (2020)
14. Liu, C.; Qiu, S.; Du, P.; Zhao, H.; Wang, L.: An ionic liquid—graphene oxide hybrid nanomaterial: synthesis and anticorrosive applications. Nanoscale **10**, 8115–8124 (2018)
15. Zhou, X.; Zhang, Y.; Huang, Z.; Lu, D.; Zhu, A.; Shi, G.: Ionic liquids modified graphene oxide composites: a high efficient adsorbent for phthalates from aqueous solution. Sci. Rep. **6**, 38417 (2016)
16. Erdenedelger, G.; Lee, T.; Dao, T.D.; Kim, J.S.; Kim, B-Su; Jeong, H.M.: Solid-state functionalization of graphene with amino acids toward water-dispersity: implications on a composite with polyaniline and its characteristics as a supercapacitor electrode material. J. Mater. Chem. A **2**, 12526–12534 (2014)
17. Kumar, A.; Khandelwal, M.: Amino acid mediated functionalization and reduction of graphene oxide—synthesis and the formation mechanism of nitrogen-doped graphene. New J. Chem. **38**, 3457 (2014)
18. Bose, S.; Kuila, T.; Mishra, A.K.; Kim, N.H.; Lee, J.H.: Dual role of glycine as a chemical functionalizer and a reducing agent in the preparation of graphene: an environmentally friendly method. J. Mater. Chem. **22**, 9696–9703 (2012)
19. Aslam, R.; Mobin, M.; Aslam, J.; Lgaz, H.; Chung, I.-M.: Inhibitory effect of sodium carboxymethylcellulose and synergistic biodegradable gemini surfactants as effective inhibitors for MS corrosion in 1 M HCl. J. Mater. Res. Technol. **8**, 4521–4533 (2019)
20. Mobin, M.; Aslam, R.; Aslam, J.: Synergistic effect of cationic gemini surfactants and butanol on the corrosion inhibition performance of mild steel in acid solution. Mater. Chem. Phys. **223**, 623–633 (2019)
21. Solomon, M.M.; Umoren, S.A.; Obot, I.B.; Sorour, A.A.; Gerengi, H.: Exploration of dextran for application as corrosion inhibitor for steel in strong acid environment: effect of molecular weight, modification, and temperature on efficiency. ACS Appl. Mater. Interfaces. **10**, 28112–28129 (2018)
22. Shoeb, M.; Mobin, M.; Ali, A.; Zaman, S.; Naqvi, A.H.: Graphene-mesoporous anatase TiO2 nanocomposite: a highly efficient and recyclable heterogeneous catalyst for one-pot multicomponent synthesis of benzodiazepine derivatives. Appl. Organomet. Chem. **32**, 3961–3979 (2018)
23. Shoeb, M.; Mobin, M.; Rauf, M.A.; Owais, M.; Naqvi, A.H.: In vitro and in vivo antimicrobial evaluation of graphene–polyindole (gr@pin) nanocomposite against methicillin-resistant staphylococcus aureus pathogen. ACS Omega **3**, 9431–9440 (2018)
24. Shoeb, M.; Singh, B.R.; Mobin, M.; Afreen, G.; Khan, W.; Naqvi, A.H.: Kinetic study on mutagenic chemical degradation through three pot synthesized graphene@ZnO nanocomposite. PLoS ONE **10**, 0135055 (2015)
25. Khan, W.; Singh, A.K.; Naseem, S.; Husain, S.; Shoeb, M.; Nadeem, M.: Synthesis and magnetic dispersibility of magnetite decorated reduced graphene oxide. Nano-Struct. Nano-Objects **16**, 180–184 (2018)
26. Jadhav, S.V.; Lee, S.H.; Nikam, D.S.; Bohara, R.A.; Pawar, S.H.; Yu, Y.S.: Studies on enhanced colloidal stability and heating ability of glycine functionalized LSMO nanoparticles for cancer hyperthermia therapy. New J. Chem. **41**, 1598–1608 (2017)
27. Antosova, A.; Bednarikova, Z.; Koneracka, M.; Antal, I.; Zavisova, V.; Kubovcikova, M.; Wu, J.W.; Wang, S.S.S.; Gazova, Z.: Destroying activity of glycine coated magnetic nanoparticles on lysozyme, α-lactalbumin, insulin and α-crystallin amyloid fibrils. J. Magn. Magn. Mater. **471**, 169–176 (2019)
28. Kumar, M.S.; Kumar, S.L.A.; Sreekanth, A.: Anticorrosion potential of 4-Amino-3-methyl-1,2,4-triazole-5-thione derivatives (SAMTT and DBAMTT) on mild steel in hydrochloric acid solution. Ind. Eng. Chem. Res. **51**, 5408–5418 (2012)
29. Ahamed, S.Z.A.; Dillip, G.R.; Raghavaiah, P.; Mallikarjuna, K.; Raju, B.D.P.: Spectroscopic and thermal studies of γ-glycine crystal grown from potassium bromide for optoelectronic applications. Arab. J. Chem. **6**, 429–433 (2013)
30. Dehghani, A.; Bahlakeh, G.; Ramezanzadeh, B.; Ramezanzadeh, M.: Potential of Borage flower aqueous extract as an environmentally sustainable corrosion inhibitor for acid corrosion of mild steel: electrochemical and theoretical studies. J. Mol. Liq. **277**, 895–911 (2019)
31. Ansari, M.M.N.; Khan, S.: Structural, electrical and optical properties of sol-gel synthesized cobalt substituted $MnFe_2O_4$ nanoparticles. Phys. B **520**, 21–27 (2017)
32. Zheng, X.; Zhang, S.; Li, W.; Yin, L.; He, J.; Wu, J.: Investigation of 1-butyl-3-methyl-1H-benzimidazolium iodide as inhibitor for mild steel in sulfuric acid solution. Corros. Sci. **80**, 383–392 (2014)

33. Yüce, A.O.; Mert, B.D.; Kardas, G.; Yazıcı, B.: Electrochemical and quantum chemical studies of 2-amino-4-methyl-thiazole as corrosion inhibitor for mild steel in HCl solution. Corros. Sci. **83**, 310–316 (2014)
34. Mobin, M.; Aslam, R.: Ester-based pyridinium gemini surfactants as novel inhibitors for mild steel corrosion in 1 M HCl Solution. Tenside, Surfactants, Deterg. **54**, 486 (2017)
35. Al-Moghrabi, R.S.; Abdel-Gaber, A.M.; Rahal, H.T.: Corrosion inhibition of mild steel in hydrochloric and nitric acid solutions using willow leaf extract. Prot. Met. Phys. Chem. Surf. **55**, 603–607 (2019)
36. Zhang, Z.; Ba, H.; Wu, Z.: Sustainable corrosion inhibitor for steel in simulated concrete pore solution by maize gluten meal extract: electrochemical and adsorption behavior studies. Constr. Build. Mater. **227**, 117080 (2019)
37. Mobin, M.; Aslam, R.: Evaluation of non-ionic surfactants as environmentally benign corrosion inhibitors for low carbon steel in 3.5 NaCl solution. Process Saf. Environ. **114**, 279–295 (2018)
38. Eddy, N.O.; Ameh, P.O.; Essien, N.B.: Experimental and computational chemistry studies on the inhibition of aluminium and mild steel in 0.1 M HCl by 3-nitrobenzoic acid. J. Taibah Univ. Sci. **12**, 545–556 (2018)
39. Aslam, R.; Mobin, M.; Zehra, S.; Obot, I.B.; Ebenso, E.E.: N, N'-Dialkylcystinegemini and monomeric N-alkyl cysteine surfactants as corrosion inhibitors on mild steel corrosion in 1 M HCl solution—a comparative study. ACS Omega **2**, 5691–5707 (2017)
40. Hoseinzadeh, A.R.; Danaee, I.; Maddahy, M.H.; Avei, M.R.: Taurıne as a green corrosion inhibitor for AISI 4130 steel alloy in hydrochloric acid solution. Chem. Eng. Commun. **201**, 380–402 (2014)
41. Solomon, M.M.; Gerengi, H.; Umoren, S.A.: Carboxymethyl cellulose/silver nanoparticles composite: synthesis, characterization and application as a benign corrosion inhibitor for St37 steel in 15% H_2SO_4 medium. ACS Appl. Mater. Interfaces. **9**, 6376–6389 (2017)
42. Cui, J.; Yang, Y.; Li, X.; Yuan, W.; Pei, Y.: Toward a slow-release borate inhibitor to control mild steel corrosion in simulated recirculating water. ACS Appl. Mater. Interfaces. **10**, 4183–4197 (2018)
43. Hsu, C.S.; Mansfeld, F.: Concerning the conversion of the constant phase element parameter Y_0 into a capacitance. Corrosion **57**, 747 (2001)
44. Saha, S.K.; Dutta, A.; Ghosh, P.; Sukul, D.; Banerjee, P.: Novel Schiff-base molecules as efficient corrosion inhibitors for mild steel surface in 1 M HCl medium: experimental and theoretical approach. Phys. Chem. Chem. Phys. **18**, 17898 (2016)
45. Fouda, A.S.; Badawy, A.A.: Adsorption and corrosion inhibition of Cu in nitric acid by expired simvastatin drug. Prot. Met. Phys. Chem. Surf. **55**, 572–582 (2019)
46. Solmaz, R.: Investigation of corrosion inhibition mechanism and stability of Vitamin B1 on mild steel in 0.5 M HCl solution. Corros. Sci. **81**, 75–84 (2014)
47. Faustin, M.; Maciuk, A.; Salvin, P.; Roos, C.; Lebrini, M.: Corrosion inhibition of C38 steel by alkaloids extract of Geissospermumlaeve in 1 M hydrochloric acid: electrochemical and phytochemical studies. Corros. Sci. **92**, 287–300 (2015)
48. Quadri, T.W.; Olasunkanmi, L.O.; Fayemi, O.E.; Solomon, M.M.; Ebenso, E.E.: Zinc oxide nanocomposites of selected polymers: synthesis, characterization, and corrosion inhibition studies on mild steel in HCl solution. ACS Omega **2**, 8421–8437 (2017)
49. Aouniti, A.; Khaled, K.F.; Hammouti, B.: Correlation between inhibition efficiency and chemical structure of some amino acids on the corrosion of armco iron in molar HCl. Int. J. Electrochem. Sci. **8**, 5925–5943 (2013)
50. Amin, M.A.; Ibrahim, M.M.: Corrosion and corrosion control of mild steel in concentrated H_2SO_4 solution by a newly synthesized glycine derivative. Corros. Sci. **53**, 873–885 (2011)
51. Eddy, N.O.; Awe, F.E.; Gimba, C.E.; Ibisi, N.O.; Ebenso, E.E.: QSAR, experimental and computational chemistry simulation studies on the inhibition, potentials of some amino acids for the corrosion of mild steel in 0.1 M HCl. Int. J. Electrochem. Sci. **6**, 931–957 (2011)
52. Zerfaoui, M.; Oudda, H.; Hammouti, B.; Kertitd, S.; Benkaddour, M.: Inhibition of corrosion of iron in citric acid media by aminoacids. Prog. Org. Coat. **51**, 134–138 (2004)
53. Zehra, S.; Mobin, M.; Aslam, J.; Parveen, M.: Assessment of glycine derivative *N*-benzylidine-2((2-oxo-2-(10H-phenothiazine-10yl)ethyl)amino) acetohydrazide as inhibitor for mild steel corrosion in 1 M HCl solution: electrochemical and theoretical approach. J. Adhes. Sci. Technol. **32**, 317–342 (2017)
54. Atta, A.M.; El-Mahdy, G.A.; Al-Lohedan, H.A.; Al-Hussain, S.A.: Application of eco-friendly magnetite nanoparticles coated with rosin amidoxime as corrosion inhibitor for mild steel in 1 M hydrochloric acid solution. Int. J. Electrochem. Sci. **10**, 2621–2633 (2015)
55. El-Mahdy, G.A.; Atta, A.M.; Dyab, A.K.F.; Al-Lohedan, H.A.: Protection of petroleum pipeline carbon steel alloys with new modified core-shell magnetite nanogel against corrosion in acidic medium. J. Chem. **2013**, 1–9 (2013)
56. Geethanjali, R.; Subhashini, S.: Synthesis of magnetite-containing polyanilinepolyacrylamide nanocomposite, characterization and corrosion inhibition behavior on mild steel in acid media. Chem. Sci. Trans. **2**, 1148–1159 (2013)
57. Atta, A.M.; El-Azabawy, O.E.; Ismail, H.S.; Hegazy, M.A.: Novel dispersed magnetite core–shell nanogel polymers as corrosion inhibitors for carbon steel in acidic medium. Corros. Sci. **53**, 1680–1689 (2011)